PHYSICAL REVIEW D VOLUME 33, NUMBER 3 1 FEBRUARY 1986

Low-energy p, $\bar{p}$, and d vertical intensities at mountain altitude

G. H. Sembroski, T. Bowen, E. W. Jenkins, J. J. Jones, and A. E. Pifer
Department of Physics, University of Arizona, Tucson, Arizona 85721

(Received 2 August 1985)

A cosmic-ray magnetic-particle spectrometer utilizing wire spark chambers and a superconducting magnet for momentum determination and scintillators for charge and velocity determination has been operated at an atmospheric depth of 747 g/cm^2. Twenty weeks of data were taken and the proton (p) energy spectrum in the momentum range of 0.6 to 2.4 GeV/c has been determined. Antiproton ($\bar{p}$) events were observed and a $\bar{p}/p$ ratio of $1.5^{+1.85}_{-0.95}$ at a momentum of 1.05 GeV/c was measured. Deuteron intensities and α-particle upper limits for this energy region are also presented.

Cosmic-ray particles have long provided both a probe of solar and galactic astrophysics and a source for the investigation of the properties of elementary particles. As a particle source, cosmic rays still retain some impressive advantages because the primary-cosmic-ray energy spectrum extends many orders of magnitude beyond that available at accelerators, up to 10^{20} eV. Intensities at these energies are extremely low, but such high energies do provide hope of being able to demonstrate unexpected new physical processes in their interactions with matter.

As an astrophysical probe, the composition of cosmic rays gives information about the source regions and the interstellar medium. Study of the spectra of the various cosmic-ray components should give insight into the mechanisms of particle acceleration and energy loss, perhaps in regions where matter under very extreme physical conditions exists. Finally, comparisons of the abundances and spectra of primary and secondary cosmic rays will provide information on their propagation through interstellar matter and through the Earth's atmosphere.

An area of great interest in cosmic-ray physics is that of the propagation of cosmic-ray primaries through interstellar and intergalactic matter. Recent measurements[1–3] have found evidence for anomalously high fluxes of $\bar{p}$'s in the primary-cosmic-ray spectrum: far too many to be accounted for by the present theories on $\bar{p}$ production from the interactions of the primary-cosmic-ray flux with interstellar matter. Many authors[4–9] have advanced new possible primary $\bar{p}$ sources to obtain enough $\bar{p}$'s to explain these measurements. An unambiguous measurement of the $\bar{p}$ flux at mountain altitude, where they are all produced by interactions of cosmic-ray particles with the atmosphere, would help greatly in determining whether the $\bar{p}$ excess found in the primary measurements was produced by interactions with the interstellar matter or originated in some unknown galactic or extragalactic source.

An experiment which would attempt to measure the $\bar{p}$ flux and perform a search for charged particles of abnormal mass must be able to sort particles by their masses. Most previous mass-sensitive particle search experiments[10–12] at sea level have used range and energy-loss techniques to determine particle energy and mass. These experiments therefore have suffered the inherent problem of ambiguous mass resolution for strongly interacting particles.

An alternative method of particle mass separation is to determine the momentum of each event by measuring its trajectory in a magnetic field and its velocity by a time-of-flight measurement. Such magnetic particle mass spectrometers have the advantage of low mass in the particle path and thus enjoy high-mass resolution for strongly interacting particles. A program of experiments of this type was initiated by the High Energy Physics Group at the University of Arizona beginning in 1973 using sophisticated accelerator techniques and equipment used by the group in its accelerator experiments. The first-generation experiment of the program[13,14] took data for one week during January of 1974 in the group's mountain-altitude laboratory. (This experiment is designated as Arizona cosmic-ray experiment I, or simply ACRE I in this paper.) The results of this experiment were very encouraging, and it was decided to perform a vastly improved second-generation version of the ACRE I experiment. The results of this second experiment (designated as ACRE II) are the basis of this work. ACRE II incorporated many significant improvements over ACRE I, including improved multiplane spark chambers to increase the particle-track-identification efficiency and more timing and charge-determination scintillation counters to improve velocity determination. Perhaps the most significant difference was the order-of-magnitude increase in statistics ACRE II achieved over ACRE I by taking data for a much longer period of time: 20 weeks for ACRE II versus 1 week for ACRE I.

This experiment was operated in the University of Arizona High Energy Physics Group's Cosmic Ray Laboratory building near the summit of Mt. Lemmon in the Santa Catalina Mountains 30 km northeast of Tucson, Arizona. The site of the laboratory building has a vertical-geomagnetic-rigidity cutoff of 5.59 GV, an altitude of 2.75 km, and an atmospheric depth of 747 g/cm^2.

EXPERIMENTAL ARRANGEMENT

The apparatus was basically a particle mass spectrometer using a superconducting magnet as an analyzing magnet, wire spark chambers for trajectory determination, and scintillation counters for velocity measurement (see Fig. 1). With this equipment, the experiment measured three quantities associated with each detected particle: the particle's trajectory in a transverse magnetic field, its time of flight between several scintillation counters, and the amount of ionization energy it deposited in each of these counters. A fourth quantity, a rough measure of the particle's range, was also measured, but this range determination was used primarily to distinguish hadrons from muons.

The trajectory information from the wire spark chambers allowed the value of a particle's rigidity, R,

$$R=\frac{P}{Z} \tag{1}$$

to be calculated. To first approximation, this rigidity can be determined by the measurement of the bend angle of the particle's trajectory through the magnetic field of the analyzing magnet:

$$R=\frac{\int \mathbf{B}\cdot d\mathbf{l}}{\theta_{\text{bend}}}, \tag{2}$$

where θ_{bend} is in radians and $\int \mathbf{B}\cdot d\mathbf{l}=92$ MeV/c for the superconducting magnet when energized to 130 A. The trajectory was determined by use of six wire spark chambers (1–6) placed almost symmetrically with three above and three below the magnet.

The velocity of each particle was determined by a group of five scintillation detectors: S1 and S2 at the top of the array, S3 directly over the magnet, and S4 and S5 near the bottom of the array (see Fig. 1). The timing of a particle's passage through these detectors was used to find its velocity, which is useful for mass determination for $\beta=v/c$ less than 0.9.

The magnitude of the charge of an event, which when used with the rigidity value gives the momentum of a particle, was determined from the pulse heights in the scintillation counters which reflect the ionization loss of a particle as it traverses each of these detectors. With the charge Z, rigidity R, and velocity β of an event known, its mass is then calculated from

$$M=\frac{ZR(1-\beta^2)^{1/2}}{\beta}. \tag{3}$$

Superconducting magnet

Momentum was found by measuring the bent trajectory of a charged particle with spark chambers before and after it passed through a region of high magnetic field. This field was provided by a superconducting magnet which was expressly built for this use at the University of Arizona and first used in the ACRE I experiment.[14,15] The magnet, Fig. 2, consisted of a superconducting

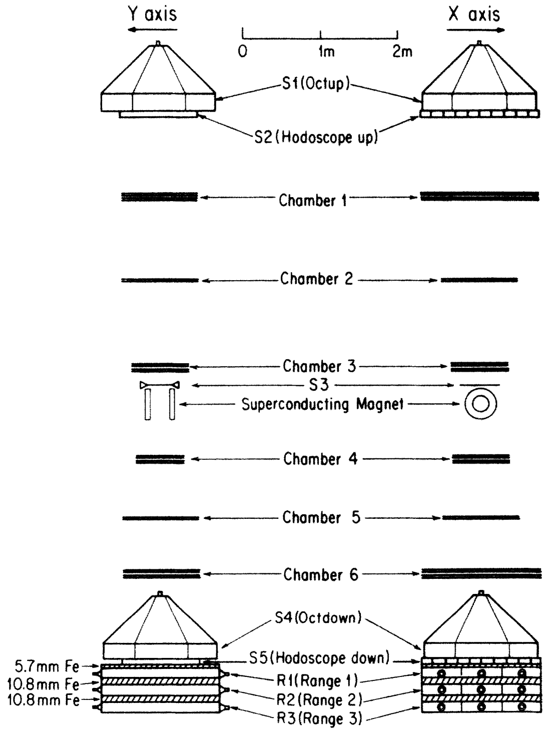

FIG. 1. Experimental arrangement: (left) view showing the y axis in which direction almost no track bending occurs in the magnetic field; (right) view showing the x axis, the magnetic-bend direction.

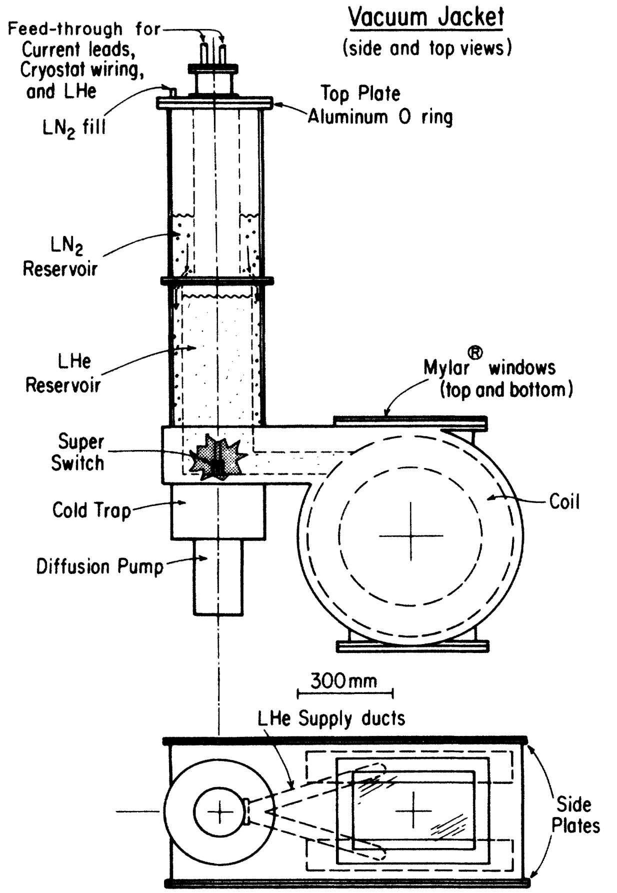

FIG. 2. Diagram of the superconducting magnet, vacuum jacket, and reservoir system. The magnet-coil assembly is suspended by stainless-steel wires.

(niobium-titanium imbedded in copper) Helmholtz-coil pair with an average radius of 18.9 cm and an average coil separation of 29.5 cm. For use during data taking, the coils were charged to a steady-state current through external leads, and then a superconducting switch was activated which shorted the leads at the coils. The complete circuit in the magnet was superconducting except for some very small resistances at joints. The field in the magnet was effectively constant with a decay time of the order of many years. At a current of 130 A, the field had a maximum strength of 17 kG and stored 500 kJ of energy. At 130 A, the magnet had an $\int \mathbf{B}\cdot dl = 2.7$ kG m for a path near the coil axis between the two coils. The liquid-helium boil-off rate was 0.28 l/h.

The magnet was run at three different current settings during the data taking, 30, 80, and 130 A, with approximately half the data taken with the current running in the opposite polarity at each of those values, but the data at 30 A was not utilized. The magnet system worked flawlessly during the 5.5 months it was energized and was allowed to warm up only when weather conditions produced snow-blocked roads, which prevented the transport of further replacement cryogenic liquids to the magnet.

In order to calculate the momentum of an event, it was necessary to know the magnetic field in all regions of the particle trajectories. The field was measured six times during the run at a large number of points on a three-dimensional lattice with 25.4-mm spacing, though not all the same points were measured each time. During operation at each current and polarity, the axial component of the field near the axis of the magnet on one lattice plane was measured frequently to provide information on the stability of the field. These measurements, with typical accuracies ~0.1%, showed no measurable decay in the field over periods of a month.

Scintillation detectors

There were four types of scintillation detectors used in this experiment (see Fig. 1). The octagonal (Oct) counters ($S1$=Octup, $S4$=Octdown) placed at opposite ends of the array were used for trigger, charge, and velocity determination. The hodoscopes ($S2$=Hodoup, $S5$=Hododown), one group placed directly under each of the Oct counters, were used for charge, velocity, and position measurements. The middle (Mid) counter ($S3$) was situated approximately halfway between the two Oct counters directly over the top magnet window and was used to ensure that the particles went primarily through this opening. The range counters ($R1$,$R2$,$R3$), placed at the very bottom of the array directly below the bottom hodoscope detector, were used to provide range information and to identify muons, a major source of background.

The construction of the Oct, Mid, and range counters was identical to that of ACRE I.[14,16] Each Hodo counter consisted of 10 independent plastic scintillation counters, each 15.2 cm wide by 5.1 cm thick by 96.5 cm long viewed at one end through a 15-cm-long tapered light pipe by an RCA 8575 photomultiplier tube. As shown in Fig. 1, these counters were oriented with the narrow, 15.2 cm, dimension in the magnetic bend (x) direction, enabling the Hodo counters to serve as a crude spectrometer, as well as detect air showers and provide timing information.

The range counters were sandwiched between layers of iron and the pulse heights were recorded. The ranges from Octdown to the three range counters along with the momenta necessary for various particles to travel these ranges are given in Table I. As can be seen, a particle would have had to traverse 299.4 g/cm^2 of copper equivalent to reach range counter $R3$. This corresponds to 3.6 nuclear collision lengths for hadrons and an initial minimum momentum of 1370 MeV/c for p's, so less than 3% would have produced a pulse in $R3$, whereas most muons with momenta >570 MeV/c are recorded in $R3$.

Spark chambers

There were six wire spark chambers (1—6) used in the ACRE II experiment, with those chambers farthest from the magnet having the largest areas to increase the geometrical acceptance. All the chambers employed magnetostrictive readout digitized with a 20-MHz clock. Single-gap chambers 2 and 5, with X and Y readouts of 0.5-mm-spaced wires, were identical to the corresponding units in ACRE I.[14] Dual-gap chambers 1, 3, 4, and 6, with X, U, V, and Y readouts of 1-mm-spaced wires, were constructed by LBL.[17] Chambers 1 and 6, measuring 1.5 m in the X direction by 1.0 m in the Y direction, had U and V planes with the wire directions rotated ±30° with respect to those in the X plane. Chambers 3 and 4, whose active areas were 45°-rotated 61-cm×50-cm rectangles covering the 22-cm×34-cm magnet vacuum chamber windows, had U and V planes with the wire directions rotated ±45° with respect to those in the X direction.

Each spark-chamber gap was pulsed with an individual 5C22 hydrogen thyratron, all of which were triggered by a Science Accessories avalanche-transistor Marx-generator pulser, as diagramed in Fig. 3. For each event, the LeCroy 801 readout system was able to digitize either 4 sparks or ≤ 3 sparks and the second fiducial. In general, the spark chambers did not work as well at the 0.72-atm pressure at the mountain laboratory as they had nearer to sea level, with a much greater tendency to exhibit spurious sparks in addition to the one produced by passage of a charged particle. The performance of chambers 2 and 5 was especially poor, so their data was ignored in most of the data analysis.

Electronics

The electronics includes a fast trigger system and a data acquisition system, as shown in Fig. 3. The trigger system was required to identify a possible good event in a

TABLE I. Range and momentum of various particles in the range-counter stack.

Range		Momentum (GeV/c)			
(g/cm^2 Cu equiv)		μ	p	d	α
$R1$	77	0.24	0.82	1.27	3.20
$R2$	188	0.41	1.14	1.73	4.53
$R3$	299	0.57	1.37	2.05	5.53

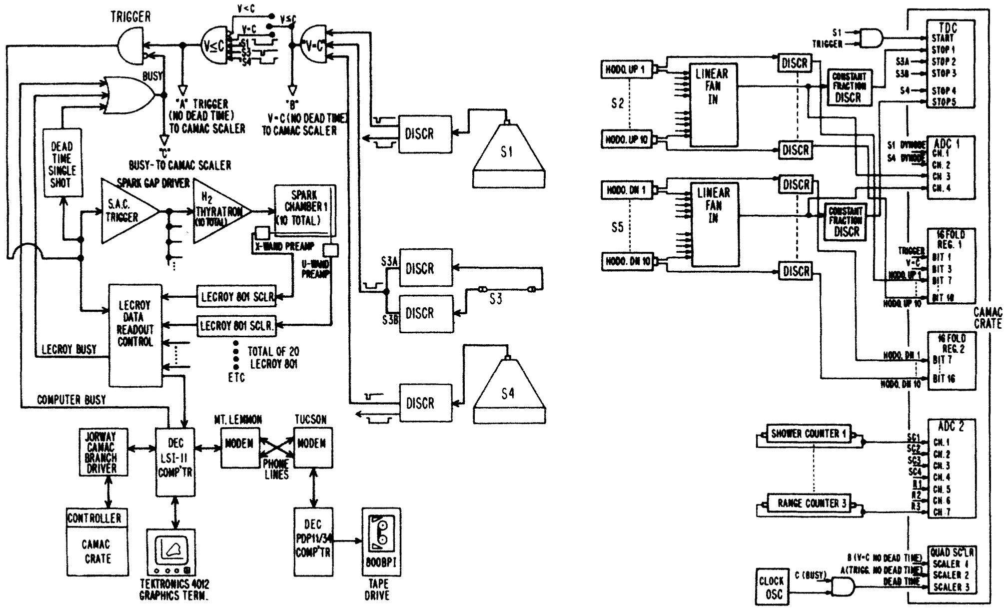

FIG. 3. Block diagram of electronics: (left) trigger system and data-acquisition computers; (right) CAMAC data-acquisition system.

time short enough (less than 100 n) to apply the high-voltage pulse to the spark chambers before the ionized track produced by the triggering particle dissipated.

The fast trigger was designed to respond only to downward-going particles which went through all six spark chambers and the windows of the magnet. Three separate triggers were available: $v=c$ ($v>0.9c$), $v\leq c$ ($v>0.28c$), and $v<c$ ($0.28c<v<0.9c$), where c is the speed of light. The trigger utilized three fast scintillation counters: S1 (Octup), S3 (Mid counter), and S4 (Octdown). The velocity determination of an event was accomplished by utilizing the timing relationships of the signals from the three counters as in ACRE I.[14] The resulting $v<c$ trigger rate (without readout dead time) was 1.5 events/s; the $v\leq c$ rate was 2.5 events/s.

Most of the data were taken using the $v<c$ trigger, since the error in calculating a mass from a velocity found from a time-of-flight error σ_t is

$$\left[\frac{\sigma_M}{M}\right]^2 \rightarrow \left[\frac{\sigma_t c}{d}\right]^2 \beta^2\gamma^4 \text{ as } \beta\rightarrow 1 , \tag{4}$$

where d is the flight distance between timing counters and $\gamma\equiv(1-\beta^2)^{-1/2}$. As the error gets very large for $\beta=v/c$ close to 1, only events with $\beta<0.9$ are of interest. The $v=c$ and $v\leq c$ triggers were employed for calibration of the system.

The data-acquisition process was controlled by a Digital Equipment Corporation (DEC) LSI 11 microcomputer interfaced to the experiment (see Fig. 3). All event information received from the two data-acquisition systems (CAMAC and LeCroy) was packed, buffered, and transmitted at 1200 baud over a dedicated phone link to a DEC PDP-11/34 campus computer located 30 km away, where the data were stored on magnetic tape. Selected parts of this data were displayed in real time in the form of scatter plots and histograms on a Tektronix 4012 graphics display terminal. The computer program also monitored various voltage levels used by the equipment in the experiment and notified the experiment operators whenever any of these levels ranged outside of previously set limits.

DATA ANALYSIS

The data-analysis process first found the momentum, velocity, and charge of each event. The calculation of each of these quantities required a detailed understanding of the particular apparatus by which it was measured. As an example, to calculate the momentum of an event, the positions of the sparks of that event had to be calculated, a track identified from this spark information, and the momentum calculated for such a track passing through the magnet. This required, among other things, knowledge of the magnetic field everywhere in the volume of space that the particle traversed, the alignment of all the chambers with respect to the center of the magnet, the distances between all the wand fiducials, and the propagation speeds in the wands. All this calibration information was derived from the raw data and was determined before calculating the momentum of any events. Similar analyses were made for the velocity and charge determinations, requiring similar parameter and calibration calculations using the raw data as the source of the necessary information.

The relative times of all pulses from $S1$–$S5$ were corrected for fixed and trajectory-dependent transit-time delays and cross compared with the help of background events due to highly relativistic ($v\simeq c$) muons, each of whose velocity and trajectory were accurately known.

The dependence of every relative time on the various delay and position parameters was investigated with the help of time versus parameter scatter plots.[18] The standard deviations of the residual errors for the hodoscope counters ranged from 0.46 to 0.8 ns, and were 0.81, 1.74, and 0.90 ns for S1, S3, and S4, respectively. The Mid counter ($S3$) was not employed for velocity measurements because it can be shown that the timing information of a counter midway between two others does not improve the statistical accuracy of the calculated delay time. However, the Mid counter is very helpful in rejecting spurious events.

The pulse heights of the Oct counters ($S1$ and $S4$) were useful in order to search for evidence of α particles ($Z=2$) in the data. Saturation corrections for scintillator light output and photomultiplier-tube (PMT) response had to be independently determined and then separately applied to each event because trajectory position affected the amount of scintillation light reaching the PMT. Slow p's provided particles with known dE/dx and trajectory. The resulting saturation curves[18] indicated that some, but not all, $Z=2$ particles would be unambiguously identifiable; however, no strong α candidate was found.

Tracks were identified by the computer by independently examining the sets of x coordinates (X track), which is the magnetic bend direction, and the sets of y coordinates (Y track), where each track should be nearly a straight line. The correspondence between X and Y tracks, when there was more than one possible pairing, was established by those x,y pairs (hits) which were linked by u or v plane coordinates.

A good Y track was defined as a track of at least three Y sparks, including at least one chamber above and another below the magnet, which fit a straight line with a maximum χ^2 per degree of freedom such that there was less than a 1% probability of exceeding that χ^2. The tracks were found using the method of stringing[19] in which the first spark (or hit) in the first chamber is taken and two lines extended from it to either side of the magnet opening (only tracks which did not go through any material in the magnet were considered). These lines were extended through the remaining five chambers and defined "search" windows in each of these chambers. The process would then continue by looking in successive chambers within their search windows for a second spark for the track. This second spark would then be incorporated in defining new and more restricted search windows. This process would continue until all six chambers were searched for sparks, and if a track with three or more sparks was found which satisfied the χ^2 criteria, it would be recorded. The sparks (and hits) in this track would then be removed from the spark arrays and the whole process repeated with the remaining sparks.

Once all the possible tracks were identified, the best and second-best tracks would be selected. The selection basis went according to the following priorities. The best track was defined as that track with the most hits. If there was a tie under this criterion, then the track with the most total number of hits plus sparks was chosen from this subset. If still more than one track fit this second criterion, then the track with the smallest χ^2 was designated as the best track. The second-best track was identified in a similar manner.

A good X-track signal required two- or three-spark line segments above and below the magnet, each having an impact parameter b_i with the magnet axis, such that $\Delta b = b_{\text{upper}} - b_{\text{lower}}$ had a magnitude $|\Delta b| < 4$ cm. The track also was required to intersect the Hodo counter, if one had triggered, and to utilize the x values of x,y "hit" pairs which belonged to the best (if none, second best) Y track.

The momentum of an event was determined by making an initial guess as to the momentum, direction, and point of entry to an array of magnetic field intensities, tracing the track of such a particle through the magnetic field array, and computing the χ^2 fit of this track to the measured data. These initial parameters were then varied until the smallest χ^2 of the calculated to the measured track was achieved. The errors in the parameters found with the χ^2 fit, especially the momentum error, came directly from the minimization algorithm.[20]

The experiment generated a total of 81 raw data tapes (with 65 000 events each) over the 5.5 months of running, of which 68 contained runs with the $v<c$ trigger (see Table II). Before being processed to find tracks, these $v<c$ events were first filtered by requiring a good event to register at least one counter in either Hodoup or Hododown (this eliminated $\lesssim 1.4\%$ of good events), but rejecting multiple track events where more than a single pair of side-by-side hodoscope counters in either Hodoup or Hododown fired (this eliminated $<1\%$ of events with

TABLE II. Data-processing statistics.

Current setting (A)	No. of tapes at this setting	No. of tapes with $v<c$ trigger data	No. of events with $v<c$ trigger	No. of $v<c$ single-track events with minimum of 1 hodoscope hit
+30	8	6	365 982	47 151
−30	6	4	242 259	23 303
+80	12	11	681 621	78 938
−80	22	18	1 060 228	91 388
+130	25	21	1 433 257	94 733
−130	8	7	422 148	19 910
Totals	87	67	4 214 495	355 423

TABLE III. Mass resolutions of proton and deuteron peaks, $\sigma(M)/M$. Equation 5(b) was fit to 80-A data.

β interval	p_p (GeV/c)	σ_p (80 A) observed	σ_p (80 A) calculated	σ_d (80 A) calculated	σ_p (130 A) observed	σ_p (130 A) calculated	σ_d (130 A) calculated
0.48—0.61	0.62	0.11	0.115	0.154	0.09	0.104	0.122
0.61—0.71	0.83	0.13	0.127	0.188	0.10	0.110	0.140
0.71—0.81	1.12	0.16	0.150	0.237	0.13	0.124	0.169
0.81—0.86	1.44	0.18	0.184	0.301	0.17	0.148	0.208
0.86—0.91	1.82	0.21	0.229	0.376	0.18	0.184	0.260

resolvable tracks). Table II lists the number of events which remained for each magnet current setting.

Mass resolution

The mass resolution is given by[14]

$$\left[\frac{\sigma_M}{M}\right]^2 = \frac{L}{L_{\text{rad}}}\left[\frac{0.015\text{ GeV}}{\int \mathbf{B}\cdot d\mathbf{l}}\right]^2 \frac{1}{\beta^2} + \frac{1}{P_{\max}{}^2}\left[\frac{M}{Z}\right]^2 \beta^2\gamma^2 + \left[\frac{\sigma_t c}{d}\right]\beta^2\gamma^4 \tag{5a}$$

$$= A\frac{1}{\beta^2} + B\left[\frac{M}{ZI_{\text{mag}}}\right]^2 \beta^2\gamma^2 + C\beta^2\gamma^4 + D\ , \tag{5b}$$

where L/L_{rad} is the thickness of the multiple-scattering material in units of the radiation length, assumed concentrated at the center of the bending magnet, $P_{\max}$ is the maximum detectable momentum, σ_t is the rms timing error, c is the speed of light, and d is the path length between time-of-flight counters. In Eq. 5(b) the parameters which depend only upon the apparatus are incorporated in the constants A, B, and C, the first term representing the multiple-scattering error, the second, the coordinate-measuring errors, and the third, the timing errors; the constant D has been arbitrarily added; and I_{mag} is the magnet current. After evaluating the timing constant $C = 0.000\,88$ from the times of flight of muons, a two-parameter fit was attempted to determine A and B from the p-mass-peak widths for β intervals 0.47—0.61, 0.61—0.71, 0.71—0.81, 0.81—0.86, and 0.86—0.91 at magnet currents of 80 and 130 A. In order to obtain a reasonable fit for A and B, it was found necessary to assume $D = 0.0073$, corresponding to a constant 8.5% random error in the bend angle of unknown origin. At this value of D, $A = 0.000\,51$, as in ACRE I,[14] and $B(M_p)^2 = 52.5$ A^2, in agreement with the bend-angle distribution of $v = c$ events at zero magnetic field. Table III shows the results when Eq. 5(b), first fitted to the 80-A data, was used to predict the mass-peak widths at 130 A for p's and d's. Typical mass distributions are shown in Fig. 4.

In the data at the 80-A magnet current, the peaks of the p mass distributions remained at a fixed position independent of β or the magnet polarity. However, in the 130-A data, the mass peak shifted as β changed, the direction of the shift being opposite for the two magnet polarities. These shifts were attributed to a change of coordinate alignment for spark chambers 3 and 4, nearest to the magnet, resulting in a constant bend-angle error; all ±130-A data were corrected for this effect.

RESULTS

Protons

The incident vertical differential momentum intensity can be written

$$I(P) = \frac{N_P}{\Delta P A\Omega(P) T\epsilon}\ , \tag{6}$$

where N_P is the net number of particles seen in the momentum interval ΔP around average momentum P during a sensitive time T for a detection apparatus which had a geometry factor $A\Omega(P)$ and a detection efficiency ϵ. Since $A\Omega(P)$, ϵ, and T were different for each polarity and setting of the current in the magnet, $I(P)$ was calculated separately for each current to confirm that the data were internally consistent. Table IV lists all the p data and parameters employed in Eq. (6).

To find the number of p's in each momentum interval (or corresponding β interval) in this experiment, histograms of the mass distributions for each interval and current were formed. Since these histograms were to be used to get absolute values of the p intensities, they had the minimum possible number of cuts. Muon contamination was negligible for $\beta < 0.81$, and was made negligible

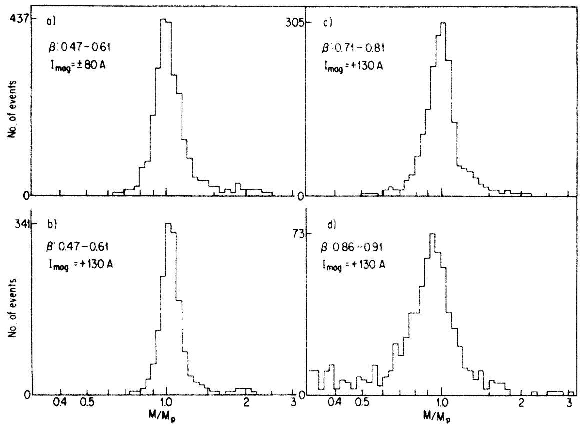

FIG. 4. Typical positive-charge mass distributions: (a) $0.47 \le \beta < 0.61$ at ±80-A magnet current; (b) $0.47 \le \beta < 0.61$ at $+130$ A; (c) $0.61 \le \beta < 0.81$ at $+130$ A; (d) $0.86 \le \beta < 0.91$ at $+130$ A.

TABLE IV. Proton intensity parameters and vertical intensities at 747 g/cm^2.

	P_p (GeV/c)	ΔP (GeV/c)	$A\Omega(P_p)$ (cm^{2}sr) 80 A	N_p	N_p	$A\Omega(P)$ (cm^{2}sr) 130 A	N_p	N_p	I_p [10^{-4} cm^{-2}sr^{-1}s^{-1}(GeV/c)$^{-1}$]
Magnet current:				+80 A	−80 A		+130 A	−130 A	
Sensitive time T:				4.13×10^5 s	6.62×10^5 s		11.95×10^5 s	2.64×10^5 s	
Efficiency ϵ:				0.40±0.05	0.36±0.06		0.25±0.05	0.27±0.04	
β interval									
0.48–0.61	0.62	0.21	25.6	1097	1467	21.1	1540	310	11.2±0.9
0.61–0.71	0.83	0.22	26.8	1226	1596	24.2	1754	441	11.6±0.9
0.71–0.81	1.12	0.35	27.7	1265	1701	26.1	1870	526	7.6±0.6
0.81–0.86	1.44	0.29	28.4	503	669	26.9	736	155	3.3±0.3
0.86–0.91	1.82	0.48	28.6	389	539	27.7	568	133	1.6±0.1
0.91–0.95	2.46	0.80	28.8	189	224	28.4	279	76	0.45±0.04

for $\beta \geq 0.81$ by rejecting all events with a pulse in range counter $R3$. The smallest possible contribution to the widths of the mass distributions due to timing errors were obtained by requiring timing information from both hodoscope detectors for each event. Since the hodoscope timing information was much better than that of the Oct counters and, more importantly, was an independent measurement of the time of flight from that used in the trigger (which used both Oct counters), only the hodoscope timing was used to calculate the velocities of these events.

The number of p's in a mass peak was determined by simply counting the number of particles in each histogram peak for $\ln(M/M_p)$ limits between -0.46 and 0.41. This logarithmic form for the mass variable was chosen since it produced more nearly Gaussian plots of the mass distribution. It is also normalized to give a value of zero for the p mass M_p. It was estimated that these limits eliminate less than 1% of the p's in any β interval, magnet polarity, or current. The backgrounds to be subtracted were determined by counting the number of events between these same limits in the histograms of negatively charged particles using the same cuts. Since these backgrounds were very small compared to the numbers in the p peaks, any corrections for charge asymmetry would be negligible.

The geometry factor $A\Omega(P)$ of each momentum interval depended on the momentum P, so a Monte Carlo calculation was carried out at 28 momenta. Above 1 GeV/c $A\Omega \simeq 29$ cm^{2}sr, independent of momentum.[18,21]

The detection efficiency ϵ was the product of the trigger efficiency, ϵ_{trig} and the spark-chamber efficiency ϵ_{ch}:

$$\epsilon = \epsilon_{\text{trig}} \epsilon_{\text{ch}} \ . \tag{7}$$

ϵ_{trig}, the fraction of all events with timing information from both hodoscopes, was 0.60 ± 0.04. ϵ_{ch} was estimated by computing the efficiency of each spark-chamber gap i by examining all tracks initially found without using the ith chamber which satisfy all the normal track criteria. It was found that the Y-track efficiency was about 95% throughout the experiment, but the X-track (bend-direction) efficiency was often below 50%. The resulting efficiency ϵ, as shown in Table IV, varied with the magnet current.

The resulting p intensities, after a weighted averaging of the results from the four magnet currents, are listed in the last column of Table IV and plotted in Fig. 5, along with data from ACRE I.[14] When the data for p spectra at all atmospheric depths are fit by a Monte Carlo calculation, such as by Barber *et al.*,[14] or to a one-dimensional diffusion equation calculation, such as by Bowen and Moats,[22] the three highest-momentum points from this experiment seem to fall too low, as shown in Fig. 5. This might be attributable to our employing a single momentum-independent efficiency factor to account for triggering and spark-chamber efficiencies. Both efficiencies may tend to fall as ionization energy losses dE/dx decrease with rising momentum, since reduced dE/dx decreases both scintillation-counter pulse heights and spark efficiencies.

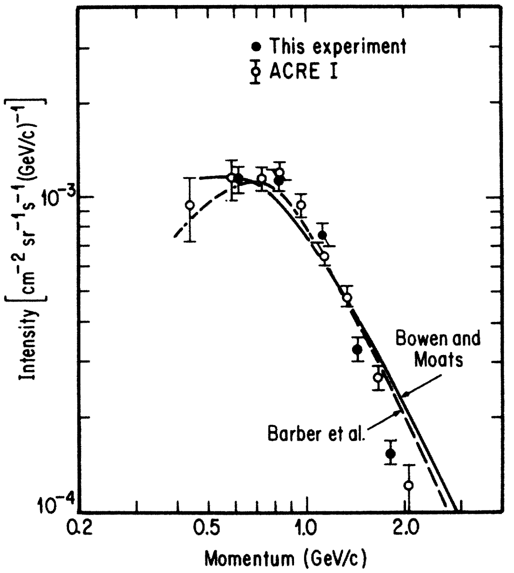

FIG. 5. Vertical proton intensities at 747 g/cm atmospheric depth. The dashed curve was obtained from a Monte Carlo calculation by Barber *et al.*, ACRE I, Ref. 14, and the solid curve from a one-dimensional diffusion calculation by Bowen and Moats, Ref. 22.

It should be stated here that while this experiment was operated at a mountain altitude corresponding to an atmospheric thickness of 747 g/cm^2, all events, in order to fit the trigger requirements, traversed an additional 21 g/cm^2 of material in the experimental array and roof of the building before entering the momentum-measuring volume of the array.

Antiprotons

Unlike p's whose signal was far above the background in the uncut data, the $\bar{p}$ signal was buried deep within it. This background consisted at high β's of mistimed muons and at low β of p's that were multiple scattered to negative angles and events which had incorrect track assignments. To reduce this background and bring out the $\bar{p}$'s, several additional cuts were made to all the data for positively and negatively charged events.

To discriminate against mistimed events, three timing cuts which used information from the Octup, Octdown, and Mid counters were utilized. Since the time of flight of a particle between adjacent Oct and Hodo counters can be neglected, the first two timing cuts compared the relative timing of each hodoscope counter to the Oct counter directly above it. The third timing cut compared the Mid counter ($S3$) timing to the appropriately weighted mean of the Hodoup ($S2$) and Hododown ($S5$). For each comparison of times t_a and t_b, $\chi^2 \equiv (t_a - t_b)^2/(\sigma_a{}^2 + \sigma_b{}^2)$ was computed; any event which exceeded the 95% χ^2 probability limit ($\chi^2 > 4.0$) in any of these three χ^2 was rejected. A further cut was made on the sum of the three χ^2 at the 95% level ($\sum_{i=1}^{3} \chi_i{}^2 > 10.5$).

Events with bad bend angles due to multiple scattering or incorrect track assignment were rejected by a series of three more cuts. For p's, the distribution of the difference in impact parameters between the upper and lower fitted X tracks, Δb, appeared to consist of two Gaussian curves of different widths, both centered at $\Delta b = 0$. By requiring $|\Delta b| \leq 1$ cm, only events in the narrow peak were accepted. This cut combined with the timing cuts reduced the number of events in the p peaks by one-third. The next two cuts were at the 95% χ^2 level on the fit of the straight Y track, and on the fit of the momentum-finding routine to the total track. These last two cuts eliminated a further 10% of the remaining events in the p peaks.

A cut applied early to all $\bar{p}$ candidates eliminated any event in any β interval which had a pulse in $R3$ in order to minimize muon contamination. While this cut had a negligible effect for p's, it may have preferentially eliminated some $\bar{p}$'s, relative to p's because some annihilation secondaries may reach $R3$, but this would only underestimate the $\bar{p}$ fluxes. The mass-distribution standard deviations σ_p were estimated for the cut-data p peak in each β interval by fitting an integral Gaussian distribution to the central two-thirds of the integral logarithmic mass distribution; they were essentially unchanged from the σ's for uncut data listed in Table III.

After applying all cuts, 21 negatively charged events remained with masses within $\pm 6\sigma_p$ of the $\bar{p}$ mass for β between 0.48 and 0.86, as shown in Fig. 6, along with the numbers of p's surviving the same cuts. The data for the 80- and 130-A magnet currents are shown separately; it is clear that the higher current, which produced greater bend angles, significantly reduced spurious background. Three clear $\bar{p}$ events are observed in the 130-A data; the probability that three such events would be selected from a random background uniformly distributed between $\pm 6\sigma_p$ which fall within ± 1.8, ± 0.9, and $\pm 0.9\sigma_p$ of the $\bar{p}$ mass is 7×10^{-3}.

The $\pm$80-A runs collected approximately twice as many p's as the $\pm$130-A runs, and, although some spurious background is present, the numbers of events within $\pm 2\sigma_p$ of the $\bar{p}$ mass corroborate the $\pm$130-A results. In fact, in the 0.71–0.81 β interval, the probability that four out of six random background events would be positioned within ± 0.1, ± 0.1, ± 0.6, and $\pm 0.9\sigma_{0=p}$ in a $\pm 6\sigma_p$ interval is 6×10^{-5}.

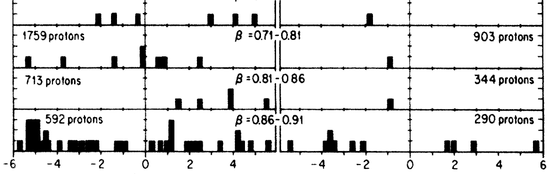

FIG. 6. Observed negative-charge events within $\pm 6\sigma_p$ of the $\bar{p}$ mass from data at $\pm$80- and $\pm$130-A magnet currents. The number of p's surviving the same analysis cuts is indicated for each velocity group.

TABLE V. Antiproton intensity parameters at 747 g/cm^2. 90%-confidence coefficient for each upper or lower limit.

β interval	$P_{\bar{p}}$ (GeV/c)	Number of p	Number of $\bar{p}$ in $\pm 2\sigma_p$	$\bar{p}/p$ ratio $(10^{-3} I_{\bar{p}}/I_p)$	$I_{\bar{p}}$ [10^{-6} cm^{-2}sr^{-1}s^{-1}(GeV/c)$^{-1}$]
0.48–0.61	0.62	2249	0	≤ 1.1	≤ 1.2
0.61–0.71	0.83	855	1	$1.2^{+3.4}_{-1.0}$	$1.3^{+3.9}_{-1.2}$
0.71–0.81	1.12	840	1	$1.2^{+3.4}_{-1.0}$	$0.9^{+2.5}_{-0.8}$
0.81–0.86	1.44	303	1	$3.3^{+9.6}_{-2.9}$	$1.0^{+3.0}_{-0.9}$
0.86–0.91	1.82	259	$0(\pm 1\sigma_p)$	≤ 13	≤ 2.1
Second, third, and fourth intervals combined:					
0.61–0.86	1.05	1998	3	$1.5^{+1.9}_{-1.0}$	$1.1^{+1.3}_{-0.7}$

The lowest interval in the combined 80- and 130-A data had no events in the $\pm 2\sigma_p$ interval around the $\bar{p}$ mass. There were 2249 p's in this β interval after all the cuts were applied. Thus an upper limit at the 90%-confidence level for the $\bar{p}/p$ ratio of 1.06×10^{-3} can be estimated for this interval. In the 0.61–0.71, 0.71–0.81, and 0.81–0.86 intervals, the 80-A data had some spurious background, and so only the 130-A data are used to calculate the $\bar{p}/p$ ratio. The highest interval, because of its large background, which included possible K^- mesons near $-3.6\sigma_p$, was used only to calculate an upper limit for the $\bar{p}/p$ ratio, based upon four events within $\pm 1\sigma_p$ of the $\bar{p}$ mass. The results of these calculations can be seen in Table V and are shown in Fig. 7. The error bars for these data designate the 90%-confidence limits. Since the p intensities are also known (Table IV), they can be used to calculate the $\bar{p}$ intensities. These intensities are also given in Table V and are further shown in Fig. 8.

As can be seen in Fig. 8, the observed $\bar{p}$ intensity is 2 orders of magnitude above the Monte Carlo calculations of Barber *et al.*[14] which used the $\bar{p}$-production cross-section estimates of Badhwar and Golden[23] to predict the $\bar{p}$ intensities at mountain altitude. These $\bar{p}$-production cross-section estimates have recently been shown to have been in error,[7] but the corrected cross sections only serve to enhance the observed disagreement between the calculated curve and the measured data. Puzzled by the apparently large discrepancy, Bowen and Moats[22] carried out an independent one-dimensional diffusion equation calculation utilizing recent $\bar{p}$-nucleus cross-section data; this curve, shown in Fig. 8, seems to be in reasonable agreement with the experimental observations. It was found that the calculated intensities deep in the atmosphere are *very* sensitive to the assumed $\bar{p}$-air annihilation and inelastic-scattering cross sections.

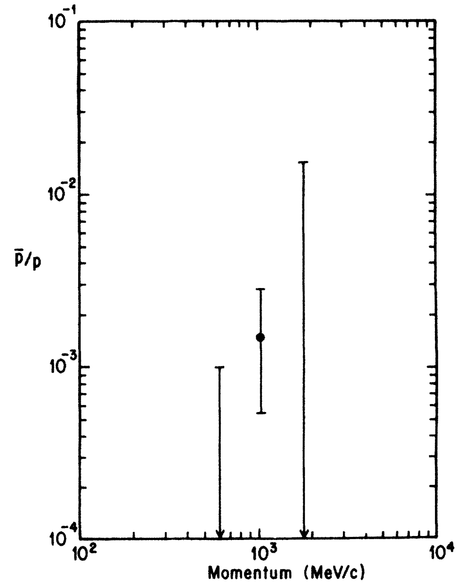

FIG. 7. $\bar{p}/p$ intensity ratios observed at 747 g/cm^2 atmospheric depth. Error bars are 90%-confidence limits.

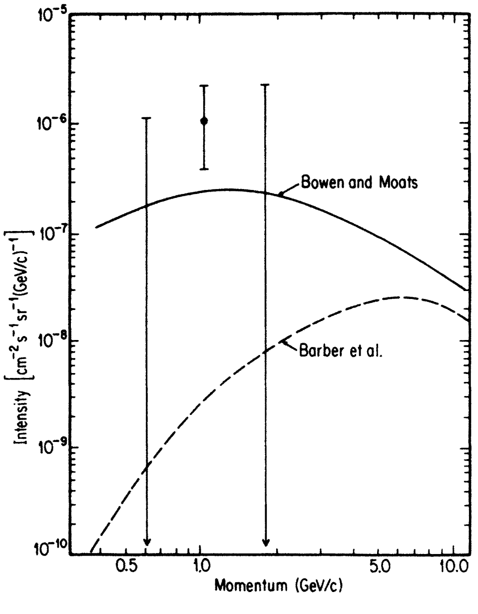

FIG. 8. $\bar{p}$ vertical intensities observed at 747 g/cm^2 atmospheric depth. Error bars are 90%-confidence limits. Curves are estimated from a Monte Carlo calculation by Barber *et al.*, Ref. 14, and one-dimensional diffusion equation by Bowen and Moats, Ref. 22.

Deuterons

The deuteron (d) mass distributions were obscured by two sources of background: randomly distributed spurious events, and the upper tail of the p mass peak. Using the logarithmic form of the mass variable, $\ln(M/M_p)$, the p peaks were centered at zero and the d's at $\ln 2 = 0.69$. Employing 130-A data to minimize p and d peak overlap, cut as described for the $\bar{p}$ analysis, the predicted d-peak standard deviations σ_d ranged from 0.12 in the $0.47 \leq \beta < 0.61$ interval to 0.26 in the $0.86 \leq \beta < 0.91$ interval. In order to remain at least $2\sigma_p$ away from the p peak, the d mass interval was originally chosen from 0.41 to $0.69 + 2\sigma_p$. Spurious d background, as indicated by the negatively charged data, was limited to one event in the 0.48—0.61 β interval, two in the 0.81—0.86 interval, four in the 0.81—0.91 interval, and none in the others. As there was still excessive overlap with the upper tail of the p distribution, only events in the upper half of the mass distribution from 0.69 to $0.69 + 2\sigma_d$ were employed to determine d/p ratios and d intensities in all but the lowest β interval. In the lowest β interval, $0.41 \leq \beta < 0.47$, the entire well-separated d peak was employed, but a d/p ratio could not be estimated because p's in this β range cannot penetrate to reach the required scintillators. The results are listed in Table VI and plotted in Fig. 9 along with earlier results and predictions from ACRE I (Ref. 14) and Kinoshita and Price.[24] In Fig. 9, all curves and data from ACRE I and II have been scaled by a factor $[\exp(-603/125)]/[\exp(-747/125)] = 3.2$ in order to normalize all data to 603 g/cm^2 depth, at which Kinoshita and Price carried out their measurements. The upper solid curve in Fig. 9 was calculated for d's by Kinoshita and Price as a refinement to the earlier dashed curve calculated by Barber *et al.*[14]

α particles

Determination of the flux of α particles was hampered by the fact that they share the same charge-to-mass ratio as d's, appearing in the mass plots (where all events were assumed to be charge $Z = 1$) in the same position as d's. To separate the α's from the d's, a Z determination for each event had to be made using the dE/dx pulse height information from the Oct and Hodoscope counters. This charge determination was difficult due to saturation effects in the photomultiplier tubes of these counters and resulted in no clearly separated $Z = 1$ and $Z = 2$ regions for the pulse-height distribution from a single counter. A plot of the hodoscope dE/dx distribution for events in the p mass peaks displayed a smoothly falling tail extending well above charge $Z = 2$. The 95% point for these plots occurred at $Z = 1.56$, which was chosen as a reasonable cutoff level.

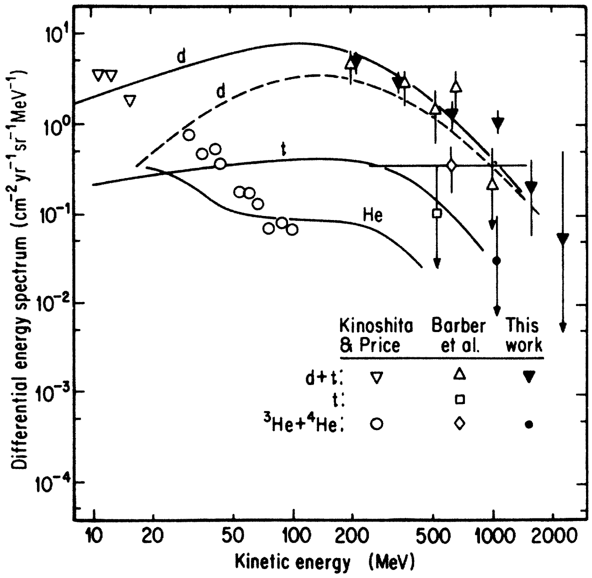

FIG. 9. d and α vertical differential energy spectra at 603 g/cm^2 atmospheric depth. Solid curves estimated by Kinoshita and Price, Ref. 24. Dashed curve estimated by Barber *et al.*, Ref. 14, for 747 g/cm^2, but scaled by a factor 3.2 to 603 g/cm^2. All experimental points above 100 MeV were measured at 747 g/cm^2 and scaled by a factor 3.2 to 603 g/cm^2.

A mass plot was made of the 130-A data which had undergone the cuts used in the $\bar{p}$ analysis and which further satisfied the following requirement: only events that had a pulse height in either Octup or Hodoup which indicated a charge greater than 1.56 and that had a pulse height in either Octdown or Hododown which also indicated a charge greater than 1.56 were included in the mass plot. Study of this mass plot revealed that the number of α candidates observed in the d mass range, when compared with the number of p's which survived the charge

TABLE VI. Deuteron vertical intensities at 747 g/cm^2 atmospheric depth. All data for d/p based upon 130-A data with $\bar{p}$ cuts. Upper limit at 90%-confidence level. The ratio d/p is for stated velocity interval, corrected by factor $(A\Omega)_p/(A\Omega)_d$.

β interval	P_d (GeV/c)	ΔP (GeV/c)	$A\Omega$ (cm^{2}sr)	Number of d-mass events Full distance	Upper half	d/p [$10^{-2} I_d/I_p$]	I_d [10^{-5} cm^{-2}sr^{-1}s^{-1} (GeV/c)$^{-1}$]
0.41—0.47	0.92	0.17	25.9	14			2.0±0.5
0.47—0.61	1.22	0.45	26.8	32	15	2.8±0.7	1.5±0.4
0.61—0.71	1.67	0.45	27.5	35	8	1.5±0.5	0.9±0.3
0.71—0.81	2.24	0.70	28.1	37	11	2.3±0.7	0.9±0.3
0.81—0.86	2.88	0.57	28.3	12	2	1.1±0.8	0.18±0.12
0.86—0.91	3.64	0.96	28.5	17	6	<6.5	<0.5

cut, was consistent with the hypothesis that the α candidates were actually d's with unusually high pulse heights in the scintillation counters. Thus, no α's were seen in the data and upper limits at the 90%-confidence level for the α/p ratios of 1.4×10^{-3} for the interval $\beta=0.48$–0.71 and 1.6×10^{-3} for the interval $\beta=0.71$–0.91 could be determined. This corresponds to upper limits of the α vertical intensities for these β intervals of

$$I_\alpha(0.48\le\beta<0.71)\le6.0\times10^{-7}\ \mathrm{cm^{-2}sr^{-1}s^{-1}}\ (\mathrm{GeV}/c)^{-1}$$

and

$$I_\alpha(0.71\le\beta<0.91)\le1.6\times10^{-7}\ \mathrm{cm^{-2}sr^{-1}s^{-1}}(\mathrm{GeV}/c)^{-1}\ .$$

The comparison of the result at the lower β interval with the result[14] of ACRE I and the calculation by Kinoshita and Price[24] is shown in Fig. 9. This upper limit from ACRE II appears to be consistent with an extrapolation of the calculated α intensity curve, and casts doubt on the events identified as α's in ACRE I.

CONCLUSIONS

Low-energy $\bar{p}$'s have been observed at mountain altitude with $\bar{p}/p$ ratios on the order of 10^{-3}. This result was surprisingly high in view of earlier predictions, but seems to agree with recent calculations for which more information was available on $\bar{p}$-air annihilation and inelastic scattering cross sections which greatly affect the slowing down of $\bar{p}$'s produced at a few GeV deep in the atmosphere. An understanding of these cross sections and the slowing-down processes occurring in the 5 g/cm^2 of interstellar matter will also affect the predictions for $\bar{p}$'s above the atmosphere, but to a much lesser degree than at 747 g/cm^2 atmospheric depth.

The p and d vertical intensities found in this experiment are in reasonable agreement with earlier results and with calculations. This provides a strong argument for the validity of the $\bar{p}$ results. The upper limits found for α intensities are consistent with calculated predictions, but bring into question the events identified as α particles by Barber *et al.*[14]

The successful operation of this superconducting-magnet, time-of-flight spectrometer indicates that an instrument of this type to measure low-energy $\bar{p}$ fluxes could be designed for balloon-borne or satellite-borne experiments. Obvious changes might include the use of multiwire proportional chambers or drift chambers instead of spark chambers for trajectory information, and Cherenkov counters instead of range counters to assist in discriminating against the high flux of relativistic particles.

ACKNOWLEDGMENTS

The authors wish to thank Niels Thompson, Michael Frey, and Ellen Cargill, who assisted with various aspects of this experiment. Dr. Paul Polakos and Dr. Donald Delise contributed major improvements to the mountain laboratory facilities as well as valuable advice. Many equipment items were loaned or contributed for this project, for which we express our appreciation to Professor A. C. Melissinos, University of Rochester, and Professor A. Wattenberg, University of Illinois, for many of the spark-chamber digitizing modules, the late Professor R. Poe, University of California—Riverside, for the hodoscope plastic scintillators, and Professor V. Perez-Mendez, Lawrence Berkeley Laboratory, for most of the spark chambers. This work was partially supported by National Science Foundation Grants Nos. PHY78-05474, PHY79-08641, and PHY82-07697.

---

[1] R. L. Golden, S. Horan, B. G. Mauger, G. D. Badhwar, J. L. Lacy, S. A. Stephens, R. R. Daniel, and J. E. Zipse, Phys. Rev. Lett. **43**, 1196 (1979).

[2] A. Buffington, S. M. Schindler, and C. R. Pennypacker, Astrophys. J. **248**, 1179 (1981).

[3] E. A. Bogomolov, N. D. Lobyanaya, V. A. Romanov, S. V. Stepanov, and M. S. Shulakova, in *16th International Cosmic Ray Conference, Kyoto, 1979, Conference Papers* (Institute of Cosmic Ray Research, University of Tokyo, Tokyo, 1979), p. 330.

[4] S. A. Stephens, Nature (London) **289**, 267 (1981).

[5] R. J. Protheroe, Astrophys. J. **254**, 391 (1982); **251**, 387 (1981).

[6] L. C. Tan and L. K. Ng, J. Phys. G **9**, 227 (1983).

[7] T. K. Gaisser and B. G. Mauger, Astrophys. J. **252**, L57 (1982).

[8] J. Szabelski, J. Wdowczyk, and A. W. Wolfendale, Nature (London) **285**, 386 (1981).

[9] P. Kiraly, J. Szabelski, J. Wdowczyk, and A. W. Wolfendale, Nature (London) **293**, 120 (1981).

[10] F. Ashton, H. J. Edwards, and G. N. Kelly, in *Proceedings of the 11th International Conference on Cosmic Rays, Budapest, 1969*, edited by P. Gombás [Acta. Phys. Acad. Sci. Hung. **29**, Suppl. 3, 327 (1970)].

[11] A. M. Galper, V. A. Gomozov, V. G. Kirillov-Ugryamov, Yu. O. Kotov, B. I. Lutchkov, and V. N. Yurov, in *Proceedings of the 12th International Conference on Cosmic Rays, Hobart, 1971*, edited by A. G. Fenton and K. B. Fenton (University of Tasmania Press, Hobart, Tasmania, 1971), p. 2317.

[12] P. C. M. Yock, Nucl. Phys. **B76**, 175 (1974); C. R. Alcock, A. Chisholm, M. Tyndel, and P. C. M. Yock, Nucl. Instrum. Methods **115**, 245 (1974).

[13] H. B. Barber, Ph.D. thesis, University of Arizona, 1976.

[14] H. B. Barber, T. Bowen, D. A. Delise, E. W. Jenkins, J. J. Jones, R. M. Kalbach, and A. E. Pifer, Phys. Rev. D **22**, 2667 (1980). The following errors should be noted: In Eq. (21) the entire denominator of the integral is carried to the 4.5 power. In Eq. (A2), the first term on the right-hand side should be $T^2p^2\sigma_\theta{}^2/Q^2$; in Eq. (A5), the right-hand side should be $0.07Q/P_{\mathrm{MD}}$; and in Eq. (A8), the right-hand side should be $a(1)/\beta^2+a(2)\beta^2\gamma^2M^2/Q^2+a(3)\beta^2\gamma^4$.

[15] N. A. Thompson, University of Arizona High Energy Physics Group Internal report, 1983 (unpublished).

[16] W. T. Beauchamp, T. Bowen, A. J. Cox, and R. M. Kalbach, Phys. Rev. D **6**, 1211 (1972).

[17] R. L. Grove, V. Perez-Mendez, and R. Van Tuyl, Lawrence Radiation Laboratory Report No. UCRL-18508, 1968 (unpublished); Nucl. Instrum. Methods **70**, 306 (1969).

[18] G. H. Sembroski, Ph.D. thesis, University of Arizona, 1983.

[19] B. G. Duff, D. A. Garbutt, R. A. Rosner, and R. N. F. Walker, Nucl. Instrum. Methods **54**, 132 (1967).

[20] P. Bevington, *Data Reduction and Error Analysis for the Physical Sciences* (McGraw-Hill, New York, 1965), p. 235.

[21] C. J. Crannell and J. F. Ormes, Nucl. Instrum. Methods **94**, 179 (1971); M. Hemmer and C. Crannell, Goddard Space Flight Center Report No. X-661-73-218, 1973 (unpublished).

[22] T. Bowen and A. Moats, following paper, Phys. Rev. D **33**, 651 (1986).

[23] G. Badhwar and R. Golden, Nature **151**, 126 (1974).

[24] K. Kinoshita and P. B. Price, Phys. Rev. D **24**, 1707 (1981).

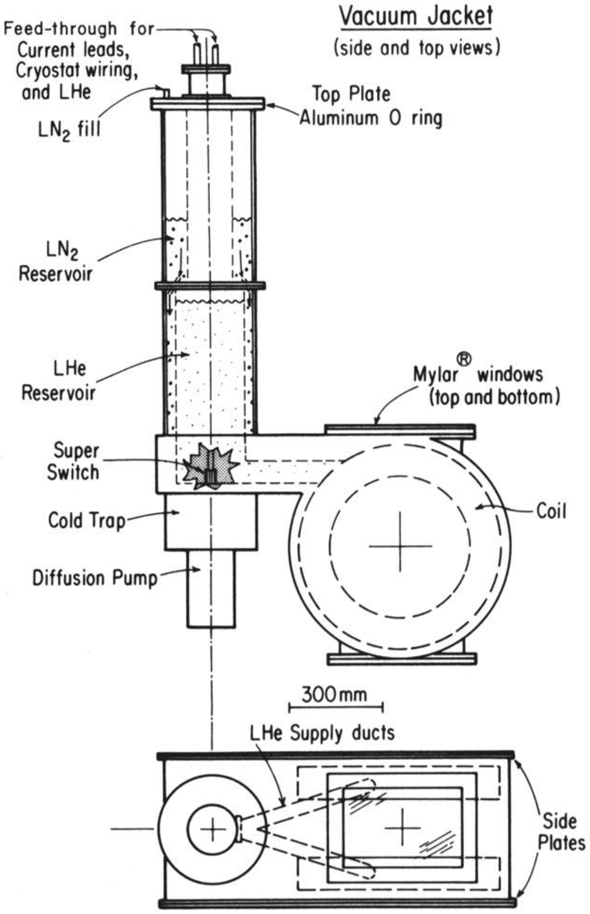

FIG. 2. Diagram of the superconducting magnet, vacuum jacket, and reservoir system. The magnet-coil assembly is suspended by stainless-steel wires.